Monthly Notices
of the
ROYAL ASTRONOMICAL SOCIETY

MNRAS **512,** 2911–2924 (2022)
Advance Access publication 2022 March 14

https://doi.org/10.1093/mnras/stac654

Non-local thermal equilibrium spectra of atmospheric molecules for exoplanets

Sam O. M. Wright, Ingo Waldmann and Sergei N. Yurchenko ★

Department of Physics and Astronomy, University College London, Gower Street, London WC1E 6BT, UK

Accepted 2022 March 2. Received 2022 February 2; in original form 2021 December 12

ABSTRACT

Here we present a study of non-local thermodynamic equilibrium (LTE) effects on the exoplanetary spectra of a collection of molecules that are key in the investigation of exoplanet atmospheres: water, methane, carbon monoxide, and titanium oxide. These molecules are chosen as examples of different spectral ranges (infrared and ultraviolet), molecular types (diatomics and polyatomics), and spectral types (electronic and rovibrational); the importance of different vibrational bands in forming distinct non-LTE spectral features is investigated. Most notably, such key spectral signatures for distinguishing between the LTE and non-LTE cases include: for CH_4 the 3.15 μm band region; for H_2O the 2.0 and 2.7 μm band regions; for TiO, a strong variation in intensity in the bands between 0.5 and 0.75 μm; and a sole CO signature between 5 and 6 μm. The analysis is based on the ExoMol cross-sections and takes advantage of the extensive vibrational assignment of these molecular line lists in the ExoMol data base. We examine LTE and non-LTE cross-sections under conditions consistent with those on WASP-12b and WASP-76b using the empirically motivated bi-temperature Treanor model.

Key words: infrared: planetary systems – methods: laboratory: molecular – molecular data – techniques: spectroscopic – planets and satellites: atmospheres.

1 INTRODUCTION

While much of the study into exoplanet atmospheres assumes species to be in local thermodynamic equilibrium (LTE), effects arising from non-local thermodynamic equilibrium (non-LTE or NLTE) are known to be present and have been detected in Earth's atmosphere, as well as the atmospheres of other Solar system planets (López-Puertas & Taylor 2001), including Venus (López-Valverde et al. 2007), Mars (López-Valverde et al. 2005), and the gas giants (Kim et al. 2015), in stellar atmospheres, comets (Weaver & Mumma 1984), and the interstellar medium (ISM; Goldsmith & Langer 1999; van der Tak et al. 2007; Lique et al. 2009). Non-LTE spectroscopy in general can be traced to Milne (1930) followed by many key papers (Curtis & Goody 1956; Houghton 1969; Kuhn & London 1969; Dickinson 1972; Kumer & James 1974; Shved 1975; López-Puertas et al. 1986a,b; Wintersteiner et al. 1992).

In addition to the importance of non-LTE effects in the spectroscopy of planetary atmospheres (López-Puertas & Taylor 2001), they have been significant in the study of stellar atmospheres for quite some time, including molecular detections such as that of aluminium oxide in the optical spectrum of VY Canis Majoris (Kaminski, Schmidt & Menten 2013a), as well as TiO and TiO_2 (Kaminski et al. 2013b). Non-LTE considerations have also played a role in constraining the abundance of SiO, CO, and HCN in the stellar envelope of R Doradus (Van de Sande et al. 2018). The roles of non-LTE effects in atomic spectra have been investigated for exoplanet atmospheres (Fisher & Heng 2019), as well as for the ion H_3^+ in giant planets within our Solar system (Drossart 2019) and extrasolar hot Jupiters (Koskinen, Aylward & Miller 2007). They have also been hypothesized to be a factor in the molecular spectroscopy of exoplanet atmospheres (Swain et al. 2010; Waldmann et al. 2012), although this has been disputed subsequently (Mandell et al. 2011). Despite this, the non-LTE spectroscopy for complex molecules in exoplanet atmospheres has not been characterized; an initial characterization of these effects in a number of the most commonly observed molecules is reported here.

A molecule is considered to be in LTE where it has equal energy in each of its modes of motion; those of vibration, translation, and rotation. In LTE a single temperature describes (i) the velocities of molecules (via the Maxwellian distribution), (ii) state populations (via the Boltzmann distribution), and (iii) ionization (via the Saha equation). In non-LTE however, this does not hold and the molecules have differing energies across their different modes. In this non-LTE regime the assumption that energy level populations can be described by the Boltzmann distribution is no longer valid. This non-LTE condition prevails where the rate of collision between molecules is insufficient to drive the molecules back to a state of LTE (i.e. with comparable energies across modes); at these collision rates, the time between collisions is greater than the time taken for de-excitation of the molecule from its non-equilibrated states. Such low collision rate conditions can be found in low-pressure regions, typically high in a planet's atmosphere (López-Puertas & Taylor 2001). For instance, CH_4 has been shown to exist in increasingly greater non-LTE for decreasing pressures below 0.1 mbar in gas giant atmospheres (Appleby 1990).

★ E-mail: s.yurchenko@ucl.ac.uk

In this paper, we examine the effects of spectral signatures indicating non-LTE populations in the atmospheres of exoplanets. To do this, we make use of the EXOCROSS software's (Yurchenko, Al-Refaie & Tennyson 2018) capability to approximate cross-sections for molecules not in LTE in conjunction with the ExoMol molecular data base (Tennyson et al. 2020).

When treated rigorously, non-LTE radiative transfer calculations solve the locally defined statistical equilibrium equations and compute the non-LTE populations of all states considered (Stiller et al. 2002; Funke et al. 2012). These calculations require a set of spectroscopic and collisional data for all molecules and states involved, which are usually only partially available. This significantly limits their application in terms of temperatures and frequencies observed. It should be noted that typical modern exoplanetary atmospheric applications cannot cope with such limitations due to large temperature ranges and comparatively low spectral resolution for space-borne observations, unsuited to populating the many parameters that are a requirement of full non-LTE population modelling. Approaching this with high-resolution spectroscopy introduces an additional limitation in discerning absolute line strengths – an important factor in distinguishing the LTE and non-LTE cases for molecular spectra. This work is an attempt to introduce a simplified, empirically motivated description of non-LTE effects in exoplanetary atmospheric retrievals. To this end, we present a detailed investigation of the contributions of different vibrational bands on forming distinct non-LTE spectral signatures for a few key molecules. As an example of such a parametrization, we explore a bi-temperature model (vibrational and rotational) sometimes referred to as the Treanor distribution (Treanor, Rich & Rehm 1968) to introduce non-LTE effects into radiative transfer calculations of exoplanets, at the molecular cross-section level. The vibrational and rotational degrees of freedom are assumed to be in their LTE (Boltzmann equilibrium; Pannier & Laux 2019), which is a common treatment in many non-LTE spectroscopic applications. Here it is common to assume the rotational degrees of freedom to be in LTE, with the non-LTE effects originating from non-Boltzmann vibrational populations obtained from statistical equilibrium equations. Such empirical evaluations are conducted in the lab, for instance using a shock region arising from a shaped nozzle, as in Dudás et al. (2020). This approximation eliminates the dependence on specific non-LTE state population ratios that could hinder achieving the aim of a comprehensive non-LTE retrieval of an exoplanet atmosphere in further work. Such a Boltzmann-like parametrization can be considered as a natural first-order approximation to the inclusion of the non-LTE populations, which would otherwise require a large amount of a priori information as input to a non-LTE radiative transfer solver (see e.g. Funke et al. 2012). Naturally the ground truths of such information are not constrained for exoplanets and the impact of seasonal and diurnal variations adds additional granularity beyond current and near-future capabilities. Instead, we approach the problem with the two-variable, bi-temperature parametrization with the non-LTE state populations having a Boltzmann-like dependence. In this way, we average most non-LTE effects into the molecular opacity tables that can then be included in retrievals.

The non-LTE effects are considered for the example of four molecules of major atmospheric importance, H_2O, CH_4, CO, and TiO, where we take advantage of the extensive vibrational assignment provided in their respective ExoMol line lists. Our formulation of non-LTE populations as molecular cross-sections approximated in this way allows us to make non-LTE spectral absorption and emission effects available to existing retrieval frameworks with little to no modification.

2 METHOD

To begin characterizing the effects of molecules in non-LTE within exoplanet atmospheres on spectra, we generated absorption cross-sections for molecules using some assumed populations $F_{J,\upsilon,k}$ of the lower states J, υ, k. For the LTE case, these are in accordance with the Boltzmann distributions for a given temperature T, as given by

$$F_{J,\upsilon,k}(T) = \frac{g^{\rm tot}_{J,k,\upsilon}\, {\rm e}^{-c_2 \tilde{E}_{J,\upsilon,k}/T}}{Q(T)}, \tag{1}$$

where $c_2 = hc/k_{\rm B}$ is the second radiation constant (cm K), $\tilde{E}_i = E_i/hc$ is the energy term value ($\rm cm^{-1}$), T is the temperature in K, and $g^{\rm tot}_{J,k,\upsilon}$ is the total degeneracy,

$$g^{\rm tot}_{J,k,\upsilon} = g^{\rm ns}_{\upsilon,k}(2J+1),$$

$Q(T)$ is the LTE partition function defined as a sum over states,

$$Q(T) = \sum_n g^{\rm tot}_{J,k,\upsilon}\, {\rm e}^{-c_2 \tilde{E}_{J,\upsilon,k}/T}, \tag{2}$$

J is the corresponding total angular momentum, $g^{\rm ns}_{J,\upsilon,k}$ is the nuclear spin statistical weight factor, and υ and k are generic vibrational (vibronic) and rotational quantum numbers, respectively.

For the non-LTE case we will assume that the rotational states can also be populated by the Boltzmann distribution corresponding to some rotational temperature $T_{\rm rot}$, which is also the kinetic temperature of the environment (López-Puertas & Taylor 2001) and the total population of J, υ, k is then approximated by a product

$$F_{J,\upsilon,k}(T_{\rm rot}) = \frac{g^{\rm tot}_{J,k,\upsilon}\, F_\upsilon\, {\rm e}^{-c_2 \tilde{E}^{\upsilon,{\rm rot}}_{J,k}/T_{\rm rot}}}{Q_{\rm rot}(T)}, \tag{3}$$

with some non-LTE vibrational populations F_υ. These non-LTE cross-sections are created using the EXOCROSS software (Yurchenko et al. 2018) with ExoMol line lists (Tennyson et al. 2020). Here the rotational energies are estimated using the following factorization:

$$\tilde{E}_{\upsilon,J,k} = \tilde{E}^{\rm vib}_\upsilon + \tilde{E}^{\upsilon,{\rm rot}}_{J,k}. \tag{4}$$

Additionally, when generating molecular cross-sections, EXOCROSS can handle the values F_υ as external parameters (Clark & Yurchenko 2021).

Expanding this to include both vibrational and rotational temperatures, in this work we use a simplified bi-temperature Treanor approximation model and investigate spectral signatures of different vibrational bands contributing to a generic non-LTE spectrum. In the Treanor approximation, the vibrational populations are modelled by a vibrational Boltzmann distribution but for a different temperature $T_{\rm vib}$, with the total non-LTE population of a given state taken as the product of the two Boltzmann distributions:

$$F_{J,\upsilon,k}(T_{\rm vib}, T_{\rm rot}) = \frac{g^{\rm tot}_{J,k,\upsilon}\, {\rm e}^{-c_2 \tilde{E}^{\rm vib}_\upsilon/T_{\rm vib}}\, {\rm e}^{-c_2 \tilde{E}^{\upsilon,{\rm rot}}_{J,k}/T_{\rm rot}}}{Q(T)}, \tag{5}$$

where $Q(T)$ is the non-LTE partition function defined as a sum over states,

$$Q(T) = \sum_n g^{\rm tot}_{J,k,\upsilon}\, {\rm e}^{-c_2 \tilde{E}^{\rm vib}_\upsilon/T_{\rm vib}}\, {\rm e}^{-c_2 \tilde{E}^{\upsilon,{\rm rot}}_{J,k}/T_{\rm rot}}. \tag{6}$$

In EXOCROSS, the vibrational part $\tilde{E}^{\rm vib}_\upsilon$ in equation (4) is taken as the lowest energy for a given υ (e.g. for $J = 0$), while the rotational contribution is then estimated via equation (4) as a difference,

$$\tilde{E}^{\upsilon,{\rm rot}}_{J,k} = \tilde{E}_{\upsilon,J,k} - \tilde{E}^{\rm vib}_\upsilon. \tag{7}$$

An absorption line intensity $I(\mathrm{f} \leftarrow \mathrm{i})$ (cm/molecule) is then given by

$$I(\mathrm{f} \leftarrow \mathrm{i}) = \frac{A_{\mathrm{fi}}}{8\pi c \tilde{\nu}_{\mathrm{fi}}^2} F_{J,\upsilon,k}(T_{\mathrm{vib}}, T_{\mathrm{rot}}) \left(1 - \mathrm{e}^{-c_2 \tilde{\nu}_{\mathrm{fi}}/T}\right), \quad (8)$$

where A_{fi} is the Einstein A coefficient (s^{-1}) and $\tilde{\nu}_{\mathrm{fi}}$ is the transition wavenumber (cm^{-1}).

As discussed in Section 1, the bi-temperature parametrization is commonly used in laboratory quantifications of non-LTE conditions. It also introduces a simplistic 'non-LTE parameter' (T_{vib}) that could be useful for atmospheric retrieval in the exoplanet case, which in a more realistic non-LTE model can be extended by introducing different T_{vib} for individual vibrational states or groups of states (López-Puertas & Taylor 2001). In the case of highly symmetric polyatomic molecules such as CH_4, such additional vibrational temperatures may be necessary to adequately describe the spectrum. For Dudás et al. (2020), a tri-temperature parametrization was necessary for CH_4: two vibrational temperatures were employed to account for differences between the stretching and bending modes of the molecule. Although this potential limitation should be borne in mind, it is worth noting that the bi-temperature model can provide sufficient descriptive performance for CH_4 in some conditions (Butterworth et al. 2020), and remains a simple method for introducing non-LTE effects where more complicated models are not possible or prohibitively difficult to compute. In addition, it can prove particularly appropriate when focusing on limited wavelength ranges, within which a particular mode dominates, reducing the need for additional vibrational temperatures.

Regardless of the model used, the non-LTE effects are largely affected by the vibrational populations of the individual states, which affect the shape of the spectrum by modifying intensities of the corresponding absorption bands. It is therefore important to characterize the individual contributions and their sensitivity to the non-LTE population input; here we make use of ExoMol state assignments to plot these individual contributions. Armed with cross-sections for molecules in LTE and non-LTE, our goal is thus to evaluate distinguishability of specific vibrational bands by evaluating the differences between the two cases; from this we can narrow down the wavelength ranges at which the differences are most apparent and with what amplitudes.

Two planets were chosen to provide reference values as case studies with which to contrast the LTE and non-LTE cases in molecular cross-sections. The WASP-12b reference case for modelling presents a target that has been well studied in the literature and is a perfect example of the extreme physical conditions that lend themselves to sustained non-LTE effects. These extreme conditions present in the atmosphere of WASP-12b include strong thermal heating and the appearance of high atmospheric inflation (Swain et al. 2013), these conditions are coupled with, and in part driven by, the planet's close proximity to its host star. This closeness also places WASP-12b in prime position for strong non-LTE conditions to arise in its atmosphere on account of stellar irradiation. The extreme conditions do not end there however, there is evidence to suggest that WASP-12b is also undergoing mass loss (Bell et al. 2019) and even that its orbit is decaying (Yee et al. 2019). WASP-76b's atmosphere was used as a template for generating TiO cross-sections due to the detection of TiO in its atmosphere (Edwards et al. 2020).

In principle it is reasonable to associate the rotational temperature to the equilibrium (kinetic) temperature. However one can also argue that the presence of non-LTE in the spectrum of an exoplanet can affect the equilibrium temperature if the retrieval model is based on the assumption of pure LTE, especially if the spectral range is very limited or due to any other shortcomings. We therefore consider two temperature scenarios when considering non-LTE spectral features. For scenario 1 the planet atmospheric equilibrium (reference) temperature (of 1864 K from Table 1 in the case of WASP-12b) was taken as the vibrational temperature (T_{vib}), while the rotational temperature (T_{rot}) was reduced to 700 K to introduce a non-LTE temperature contrast between the two temperatures. For scenario 2, the equilibrium atmospheric temperature was taken as the rotational temperature (a common assumption in non-LTE atmospheric studies) on account of the fast equilibration times of the rotational degrees of freedom. The vibrational temperature is increased symmetrically with the decrease in scenario 1 (such that it is 3028 K in scenario 2, in line with dayside temperatures retrieved in the literature; Swain et al. 2013; Arcangeli et al. 2021).

WASP-76b is also considered for scenario 1 in order to examine cross-sections for TiO (since it has been detected in the literature), with a rotational temperature of 1800 K taken along with the equilibrium temperature of 2231 K from Table 1 as the vibrational temperature. This gradient of 431 K is conservative when compared to dayside–nightside differences found from phase curves in the literature (May et al. 2021), correspondingly the vibrational temperature is raised to 2662 K under scenario 2.

These non-LTE bi-temperature cross-sections are then compared to baseline LTE cross-sections for temperatures based on the reference exoplanet atmospheres.

Table 1. Parameters used to inform cross-section calculations.

Parameter	WASP-12b	WASP-76b
Planet radius (R_{J})	1.9	1.854
Planet mass (M_{J})	1.47	0.894
Planet equilibrium temperature (K)	1864	2231
Stellar temperature (K)	6360	6329
Stellar radius ($\mathrm{R}_{\odot}$)	1.657	1.756
Cloud log pressure (Pa)	2.38	8.128
H_2O log mixing ratio	−3.12	−2.85
CO_2 log mixing ratio	−9.00	–
TiO log mixing ratio	–	−5.62
Transit duration (h)	3.00	3.69
Stellar log g ($\mathrm{cm\ s}^{-2}$)	4.15	4.196
Stellar metallicity (dex)	0.3	0.23
Inclination	83.37	89.623
Semimajor axis (au)	3.039	0.0334
Period (d)	1.091	1.8099

3 CASE STUDIES

For the molecules considered in this paper (CH_4, H_2O, CO, and TiO) we primarily examine cross-sections directly, using reference temperatures from WASP-12b and WASP-76b for two non-LTE scenarios. Although molecular non-LTE examples for atmospheres within our Solar system are commonly seen in emission, the choice to explore these effects on absorption cross-sections is motivated by demonstrating the application to exoplanet atmosphere retrieval codes. These codes ingest absorption cross-section data for use in the modelling of exoplanet atmospheres. These allow us to see how individual absorption transitions originating from over- or underpopulated lower vibrational states affect the molecular absorption due to non-LTE effects. Individual vibrational bands are characterized by different shapes, which are independent from the LTE or non-LTE model. Their spectral mixture is however defined by the specific set of the (ro)vibrational populations. These shapes are distinct even

at low resolution due to their broad natures and can be used as indicators of the presence of (specific) non-LTE effects. In this work, the individual vibrational bands are generated as absorption cross-sections with the help of the vibrational quantum numbers provided in the ExoMol line lists. The bi-temperature non-LTE models with the high-contrast temperatures described above present a convenient tool to visualize the signatures of possible non-LTE vibrational effects.

Examining the raw molecular cross-sections and identifying the distinctions between the LTE and non-LTE cases are necessary to identify non-LTE 'signatures'. These signatures represent the ideal scenario of distinguishing non-LTE from LTE at the raw cross-section level; this is before additional atmospheric factors are accounted for by forward modelling, and without considering instrument limitations. In some cases large differences in the spectra are observed that may be visible at lower resolution and in some cases there are also many individual lines that differ between the LTE and non-LTE spectra; such differences in the individual lines may be resolvable with high-resolution spectroscopy performed from the ground. In these cross-sections, we can first identify non-LTE signatures where the spectrum for a given molecule in non-LTE differs from that of the same molecule in LTE.

3.1 Absorption water cross-sections

The difference in the non-LTE and LTE spectra of water can be illustrated by analysing intensities of the individual vibrational bands. Indeed, according to equation (5) and also assuming that the non-LTE rotational temperature matches the LTE equilibrium temperature (scenario 2: $T_{\rm rot} = T_{\rm eq}$), a non-LTE spectrum can be understood as a combination of vibrational bands that correspond to higher vibrational temperatures. Under the LTE conditions, only the lowest vibrational states are significantly populated, with the vibrational ground state the most populated, and, depending on energies and temperature, the first excited vibrational states. In the case of the H_2O molecule these are ν_1 (symmetric stretch), ν_2 (symmetric bend), and ν_3 (asymmetric stretch), where the energy of ν_2 is almost half of ν_1 or ν_3. A non-LTE spectrum with a higher vibrational temperature ($T_{\rm vib} > T_{\rm rot}$) contains transitions corresponding to excited vibrational states beyond the ground vibrational state.

Fig. 1 shows cross-section contributions from several vibrational bands of H_2O plotted on top of each other, both for the LTE and non-LTE absorption spectra, where the latter are given for both scenario 1 and scenario 2. The LTE spectrum was computed using $T = 1864$ K, while the non-LTE spectra correspond to $T_{\rm rot} = 700$ K and $T_{\rm vib} = 1864$ K for scenario 1 and $T_{\rm rot} = 1864$ K and $T_{\rm vib} = 3028$ K for scenario 2, all with pressure broadening consistent with 1 bar atmospheric pressure. Different colours represent bands originating from different lower vibrational states (v_1, v_2, v_3), where v_1, v_2, and v_3 are the standard normal mode quantum numbers corresponding to the (lower state) symmetric stretch, symmetric bend, and asymmetric stretch, respectively. For example, $(1, 0, 0) \leftarrow (0, 0, 0)$ corresponds to the fundamental band v_1, which originates in the ground vibrational state, while $(1, 1, 0) \leftarrow (0, 1, 0)$ is an example of a hot band originating in the vibrationally excited state (0,1,0). Only quantum numbers of the lower states (v_1, v_2, v_3) are indicated in this figure.

As expected, the LTE spectrum of H_2O at $T = 1864$ K in Fig. 1 is dominated by the overtone bands starting from the ground vibrational state (0, 0, 0) with some contribution from the hot band originating from the bending state (0, 1, 0). The latter has a similar profile and therefore does not affect the overall shape of the spectrum.

In the case of the $T_{\rm rot} = 700$ K, $T_{\rm vib} = 1864$ K non-LTE simulations (scenario 1), the contributions from the hotter bands become significant. What is important here is that the stretching excitations are characterized by different profiles. As a result, the change becomes significant even for lower resolutions. For example, strong structures at 1.4 or 1.95 μm come from the hot bands solely due to the non-LTE vibrational excitations of $T_{\rm vib} = 1864$ K. The contribution to the signature non-LTE shoulder can be seen most distinctly in Fig. 1 where the excited bands cause substantial divergence from the LTE case between 1.9 and 2.05 μm.

When considering the second non-LTE scenario, i.e. for $T_{\rm rot} = 1864$ K, $T_{\rm vib} = 3028$ K, the differences become even more apparent. Comparing the bottom panel of Fig. 1 to the middle panel, the additional contributions to the spectra of states other than the ground vibrational state (0, 0, 0) are shown to be in excess for scenario 2.

Fig. 2 compares opacity cross-sections for H_2O in LTE and non-LTE at WASP-12b's equilibrium temperature (1864 K) and a pressure of 1 bar, with a rotational temperature of 700 K for the non-LTE case assuming scenario 1 (reduced $T_{\rm rot}$). This is a large temperature contrast case chosen to demonstrate non-LTE effects that can arise in exoplanet atmospheres. For H_2O, as shown in Fig. 2, the characteristic difference between the non-LTE and LTE cases is 'shoulders' present where H_2O is in LTE, but absent when in non-LTE, which are also shown in Fig. 2 (left display) as a zoom-in of the 1.4 μm band. These shoulders are formed from the rotational structure of a given vibrational fundamental band, i.e. having originated in the ground vibrational state. They are predominantly from the (0, 1, 0), (0, 2, 0), and (0, 3, 0) bands and are thus characteristic for the rotational temperature. The narrowing of the shoulders in the case of a lower rotational temperature can be significant and thus represents the characteristic non-LTE signature. The detection potential is greatest in the infrared (IR) region of the electromagnetic spectrum; at wavelengths below this – in the optical – absorption is too low to be visible above other atmospheric effects, such as Rayleigh scattering. In addition to sufficient absorption by the molecule in the IR, the greatest departures from the LTE case occur here. LTE and non-LTE cross-sections are contrasted for the second non-LTE scenario in Fig. 4; under this scenario, distinctions between the two cases remain although they are less pronounced and so to distinguish the two cases requires focusing on the bands below 2 μm.

Fig. 3 focuses on the 1–5 μm range for scenario 1 that encompasses multiple H_2O absorption bands used in constraining the abundance of water in exoplanet atmospheres. In this wavelength range the shoulders that form the divergence between the LTE and non-LTE cases can be clearly seen when viewing both cases overplotted, as shown at $R \sim 15\,000$ in Fig. 2 and down-binned to $R \sim 150$ in Fig. 3. The relative differences plotted in the lower segment of Fig. 3 show absorption diverging from the LTE case by as much as 1.74× at the band around 3 μm, while for scenario 2 Fig. 5 shows relative differences that can exceed 1.6×, albeit with a lower overall intensity in the nearer IR. Despite harbouring differences of a greater magnitude, the low absorption in these troughs is particularly susceptible to obstruction by cloud layers in a planet's atmosphere. The *Hubble Space Telescope* is predisposed to the detection of water owing to the wavelength coverage of its Wide Field Camera 3; in considering its potential for observing a distinct non-LTE signature this wavelength range can be seen in Figs 2 and 4 at $R \sim 15\,000$. The corresponding differences for H_2O under our second scenario are shown in Fig. 5. Although not as pronounced, differences remain by which the non-LTE case can be distinguished from the LTE one. These are most visible at the lower wavelengths, for instance in the wavelength range between 1.1 and 1.6 μm as shown in Fig. 5, left-hand panel, where a flip of the shoulders now gives the non-LTE case a broader profile when vibrationally excited, compared to the rotational cooling in scenario 1.

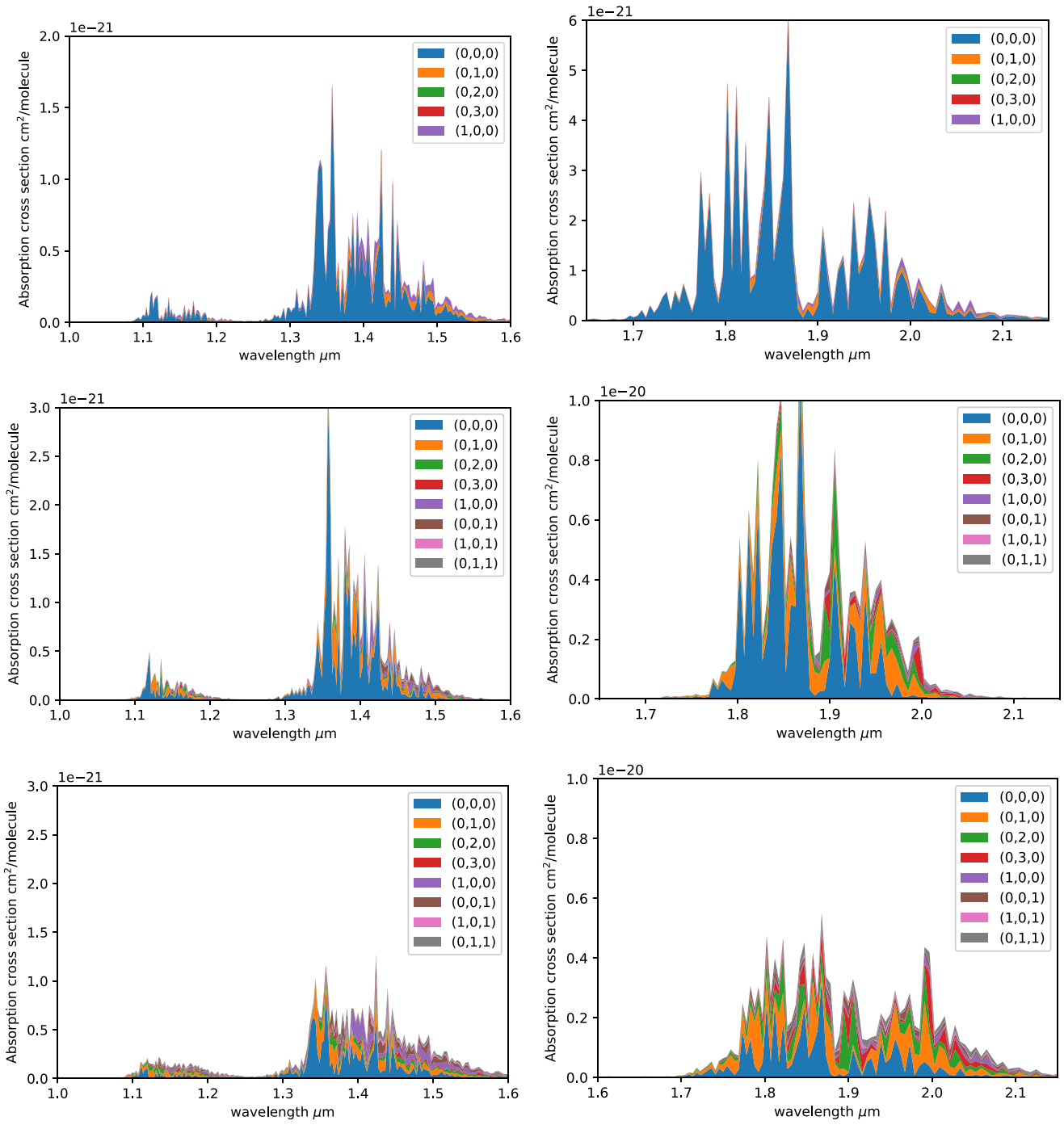

Figure 1. The individual contributions to the $2\nu_2$ (left-hand column) and $\nu_1 + \nu_2$ (right-hand column) systems from different absorption bands for H_2O at 1 bar pressure. Shown for: LTE ($T = 1864$ K; top row), non-LTE scenario 1 ($T_{rot} = 700$ K, $T_{vib} = 1864$ K; middle row), and non-LTE scenario 2 ($T_{rot} = 1864$ K, $T_{vib} = 3028$ K; bottom row). Legends indicate quantum numbers (v_1, v_2, v_3) of the lower vibrational states.

3.2 CO cross-sections

The CO cross-sections are calculated from the Li line list (Li et al. 2015) with Voigt line profiles at a resolution of ∼15 000, run across a vibrational temperature grid spanning 100–3400 K at increments of 100 K. The wide ranging degree to which the CO molecule absorbs, down to less than 10^{-100} cm^2 per molecule, leaves only a few bands visible over other contributions in atmospheric spectra. The result is that we are only interested in a few bands; all located below 7 μm when we constrain to a log absorption greater than −28. These are shown in Fig. 6. Of these three bands the most absorbing one lies at 5 μm, in addition to this it presents a candidate for distinguishing the LTE and non-LTE cases owing to the offset trailing edge of the band for CO in LTE.

Using our first scenario, the non-LTE cross-absorptions are generated using the bi-temperature model set with the rotational temperature as 700 K and the vibrational temperature as 1864 K,

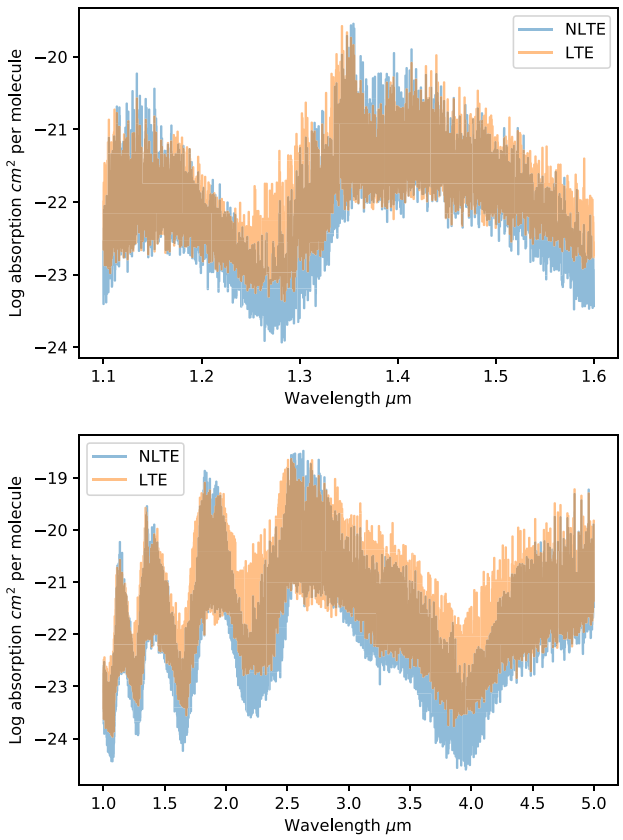

Figure 2. Opacity cross-sections for H_2O in LTE and non-LTE at WASP-12b's equilibrium temperature (1864 K) and a pressure of 1 bar, with a rotational temperature of 700 K for the non-LTE case in the 1.1–1.6 μm region (top display) and 1–5 μm region (bottom display).

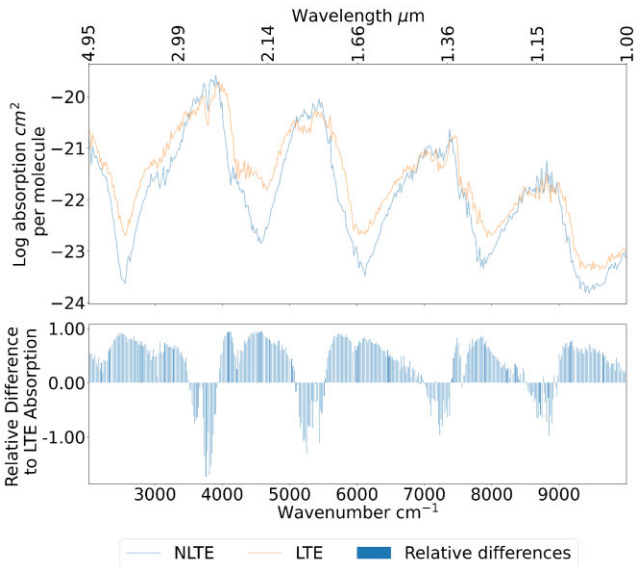

Figure 3. Opacity cross-sections in the 1–5 μm region for H_2O in LTE and non-LTE at WASP-12b's equilibrium temperature (1864 K) and a pressure of 1 bar, with a rotational temperature of 700 K for the non-LTE case. Down-binned to the resolving power of $R \sim 150$ with the difference in absorption relative to the LTE case plotted beneath.

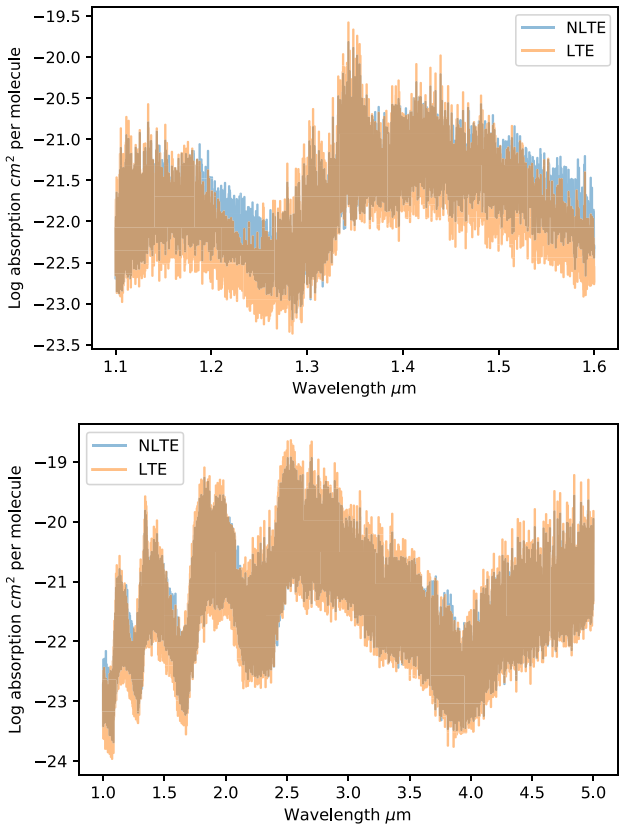

Figure 4. Opacity cross-sections for H_2O in LTE and non-LTE at WASP-12b's equilibrium temperature (1864 K) and a pressure of 1 bar, with a vibrational temperature of 3028 K for the non-LTE case in the 1.1–1.6 μm region (top display) and 1–5 μm region (bottom display).

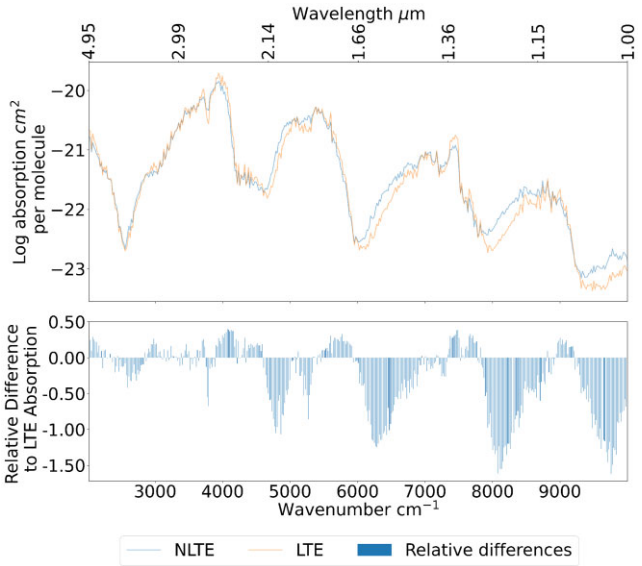

Figure 5. Opacity cross-sections in the 1–5 μm region for H_2O in LTE and non-LTE at WASP-12b's equilibrium temperature (1864 K) and a pressure of 1 bar, with a vibrational temperature of 3028 K for the non-LTE case. Down-binned to the resolving power of $R \sim 150$ with the difference in absorption relative to the LTE case plotted beneath.

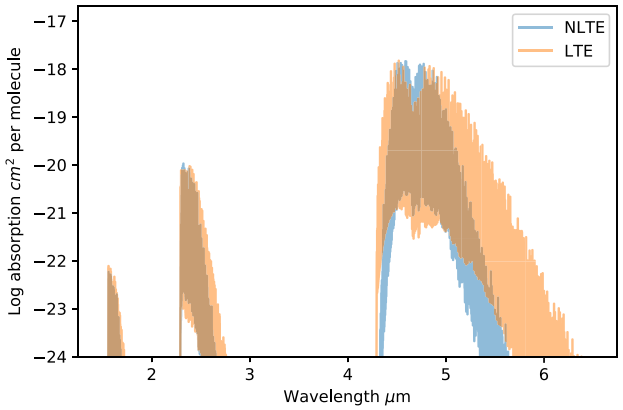

Figure 6. Opacity cross-sections for CO in LTE (1864 K) at WASP-12b's equilibrium temperature and non-LTE ($T_{\rm rot}$ = 700 K, $T_{\rm vib}$ = 1864 K) for scenario 1, with pressure of 1 bar at $R \sim 15\,000$.

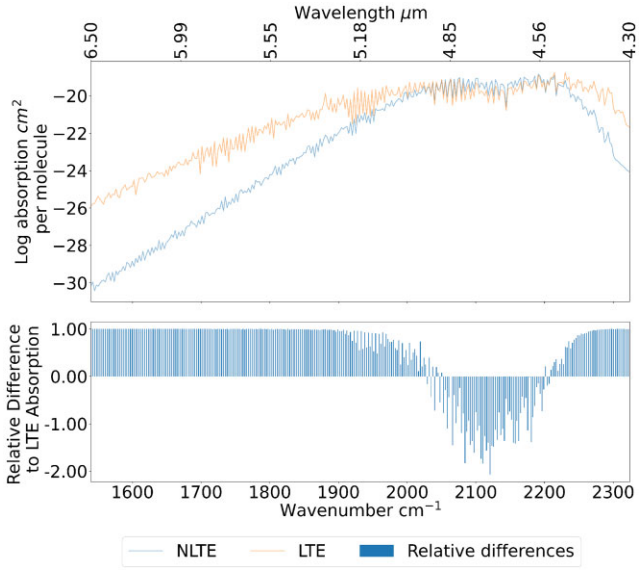

Figure 7. Opacity cross-sections focusing on the prominent band for CO in LTE and non-LTE at WASP-12b's equilibrium temperature (1864 K) and a pressure of 1 bar binned down to $R \sim 1500$ for clarity, with a rotational temperature of 700 K for the non-LTE case, in line with scenario 1.

WASP-12b's equilibrium temperature. This third band is the focus of Fig. 7 that shows a sizeable difference of up to 4.49× between the LTE and non-LTE cases for CO absorption in the (wavelength) band peak. In this band we can also observe a band shift where the non-LTE intensity drops off abruptly compared to the LTE intensity, this contraction of the edge presents a good opportunity to identify carbon monoxide in non-LTE.

An offset can also be seen under scenario 2 ($T_{\rm rot}$ = 1864 K, $T_{\rm vib}$ = 3028 K) in Fig. 8, although the difference at 6 μm is not as great as in scenario 1, the distinction at lower wavelength bands becomes far more useful: at 3 μm a larger offset emerges for scenario 2 than the much smaller offset, with a great deal of overlap, that is present in the scenario 1 case.

To demonstrate that these differences persist at low pressures, such as those in low-pressure atmospheric regions where we expect to find persistent non-LTE effects, the CO LTE and non-LTE cases are plotted in Fig. 9 for a pressure of 10^{-4} bar (Swain et al. 2010). In

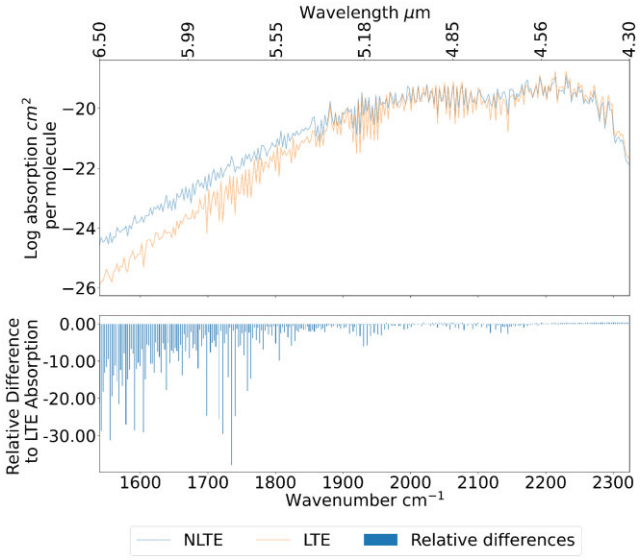

Figure 8. Opacity cross-sections for CO in LTE and non-LTE at WASP-12b's equilibrium temperature (1864 K) and a pressure of 1 bar at $R \sim 1500$, with a vibrational temperature of 3028 K for the non-LTE case, to demonstrate the non-LTE effect in our second scenario.

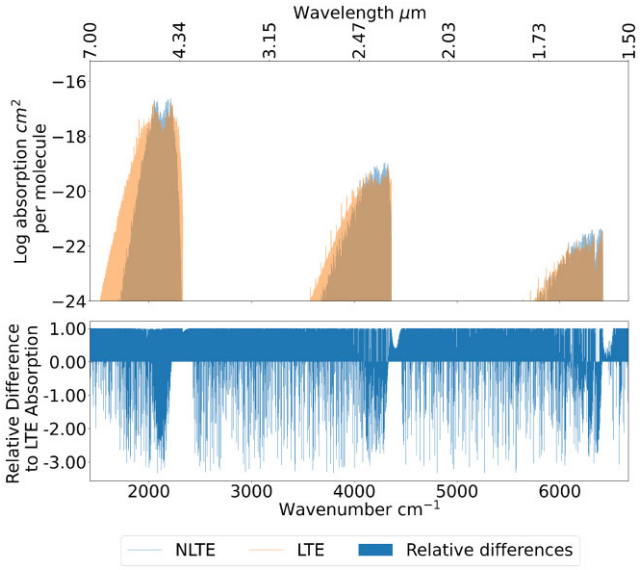

Figure 9. Opacity cross-sections for CO in LTE and non-LTE at WASP-12b's equilibrium temperature (1864 K) and a pressure of 10^{-4} bar at $R \sim 150\,000$, with a rotational temperature of 700 K for the non-LTE case, as we define in scenario 1.

addition, this plot shows the cross-sections at a resolution of 150 000 (in line with the resolving power of the CRIRES + instrument) to demonstrate the application to high-resolution spectroscopy.

3.3 Methane cross-sections

The non-LTE opacity cross-sections were generated using the ExoMol CH_4 line list 10to10 (Yurchenko & Tennyson 2014) at 1 bar of pressure, a resolution of ∼15 000. Fig. 10 shows the absorptions and differences between them for methane in LTE (T = 1864 K) and non-LTE under non-LTE scenario 1 (700 K/1864 K). In the mid-IR we see relative differences in intensity between 1.8× for the band

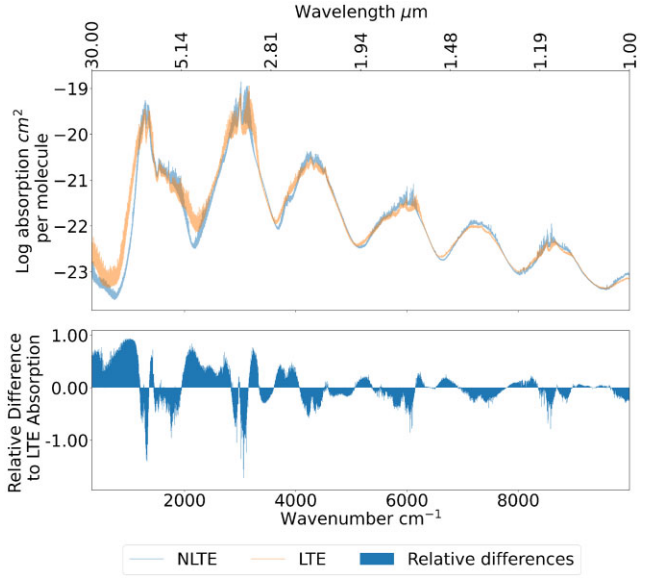

Figure 10. Opacity cross-sections for CH_4 in LTE and non-LTE at WASP-12b's equilibrium temperature (1864 K) and a pressure of 1 bar, with a rotational temperature of 700 K for the scenario 1 non-LTE case. At $R \sim 15\,000$.

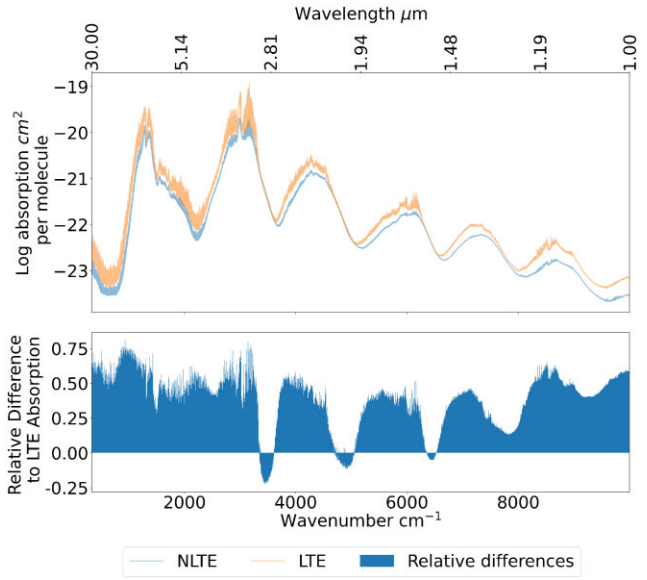

Figure 11. Opacity cross-sections for CH_4 in LTE and non-LTE at WASP-12b's equilibrium temperature (1864 K) and a pressure of 1 bar, with a vibrational temperature of 3028 K for the scenario 2 non-LTE case. At $R \sim 15\,000$.

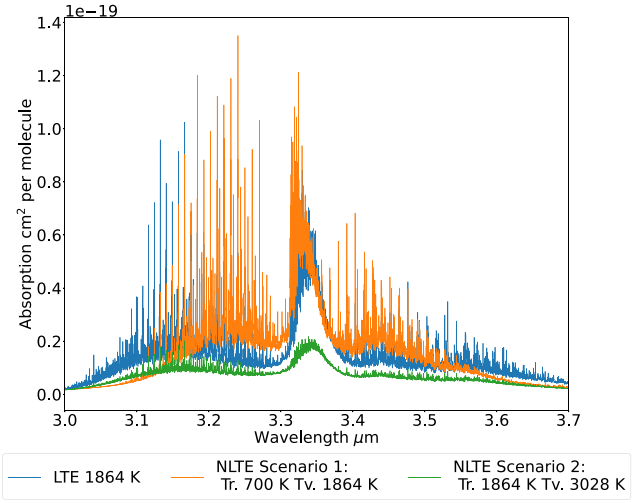

Figure 12. Opacity cross-sections for the band centred around 3.3 μm of CH_4 in LTE and non-LTE at WASP-12b's equilibrium temperature (1864 K) and a pressure of 1 bar, with a rotational temperature of 700 K for the scenario 1 non-LTE case and a vibrational temperature of 3028 K for the scenario 2 non-LTE case. Shown at $R \sim 15\,000$.

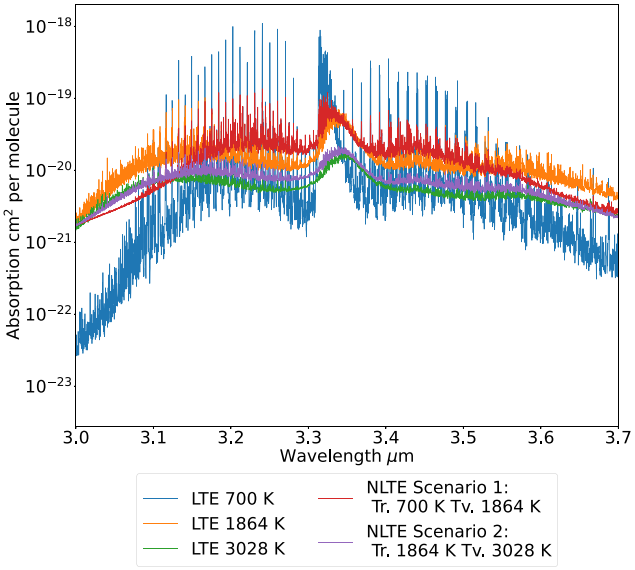

Figure 13. Opacity cross-sections of CH_4 for the two non-LTE scenarios for the band centred around 3.3 μm at $R \sim 15\,000$. In addition, three LTE baselines are shown, one for each temperature used in generating the cross-sections.

around 3 μm. When considering wavelengths above 5 μm, such as will be probed by the *James Webb Space Telescope* (*JWST*)'s Mid-Infrared Instrument (MIRI), these relative differences in intensity climb as high as 1.55× and there are substantial wavelength offsets that differentiate the LTE and non-LTE cases. Substantial differences can also be seen under scenario 2 as in Fig. 11, the absorption damping relative to the LTE case gives rise to persistent differences between the two sets of cross-sections, most notably above 2.8 μm.

Isolating the band centred around ∼3.3 μm in Fig. 12 shows differences around this band peak; for the scenario 1 non-LTE case this is characterized by a tighter profile when compared to LTE. At peak absorption this can be seen in a wavelength offset of 0.1 μm. The *R* branch is blueshifted in the case of non-LTE by ≈0.0453 μm. Under the second scenario, the non-LTE case is damped with lower absorption than the LTE case.

It can be seen from Fig. 13 that, regardless of the reference temperature chosen (be it the equilibrium temperature or the cooled rotational temperature or the excited vibrational temperature), there are still noticeable differences between both non-LTE scenarios and each LTE baseline.

Fig. 14 offers a detailed illustration of a non-LTE spectrum of CH_4 as formed from individual vibrational bands. The main contribution

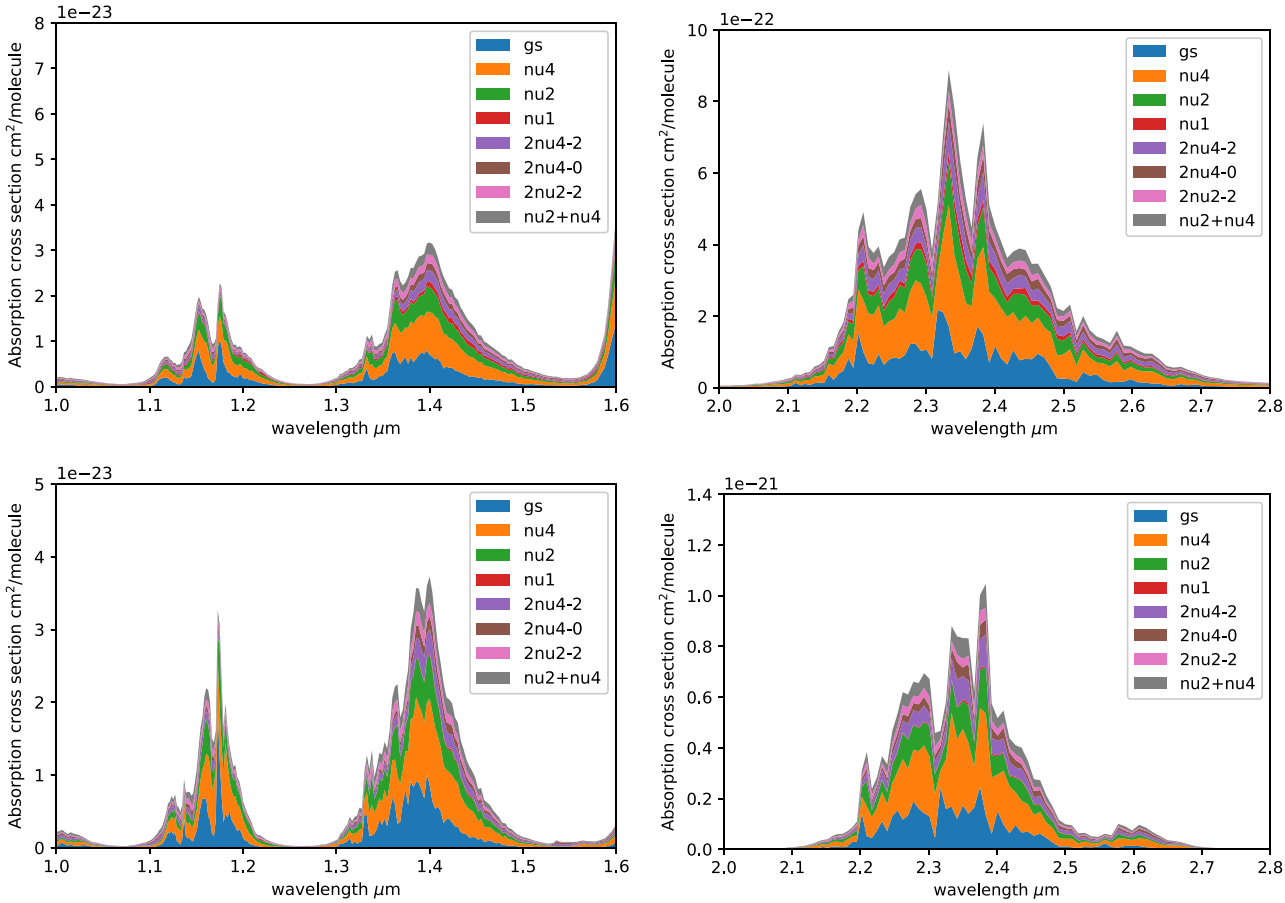

Figure 14. The individual contributions to the 1.18, 1.4, and 2.4 μm systems of CH_4 from different absorption bands, LTE and non-LTE (top two and bottom two panes, respectively). Legends indicate lower vibrational states.

to the LTE spectrum comes from fundamental/overtone bands (i.e. vibrational bands originating from the ground vibrational state) and from the singly excited bending modes ν_2 (doubly degenerate) and ν_4 (triply degenerate). The latter are characterized by relatively low energies (1533.3 and 1310.8 cm^{-1}, respectively). The elevated non-LTE vibrational populations of the other excited states correspond to the elevated vibrational temperature (here $T_{vib} = 1864$ K) providing a sizeable change to spectral composition and consequently to the overall spectral shape. The strongest features in non-LTE appear sharper and even shift their positions, see Fig. 14. The spread of different bands is defined by intensities of the individual rotational lines and is therefore controlled by the same rotational temperature. When placed on top of each other, as in the case of CH_4 or H_2O (Fig. 1), the hot bands increase the vertical magnitude of the spectral shape while leaving the horizontal spread practically unchanged. This appears to be a general property of the (IR) spectra of non-linear polyatomic molecules, with their hot bands growing on top of each other.

To demonstrate the presence of these differences at the low pressures where these non-LTE effects occur, the cross-sections for CH_4 are plotted for a pressure of 10^{-4} bar in Figs 15 and 16 for scenario 1 and scenario 2, respectively. These differences are quantified in Figs 17 and 18. In addition, these plots show the absorption intensity across wavelength at a resolution of $R \sim 150\,000$, as may be required for high-resolution applications.

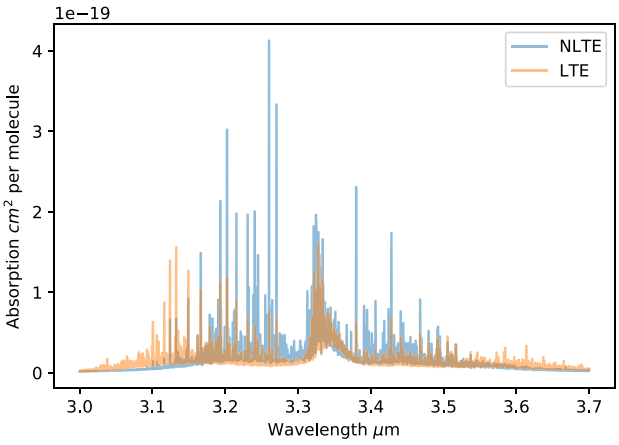

Figure 15. Opacity cross-sections of CH_4 for the first non-LTE scenarios for the band centred around 3.3 μm at $R \sim 150\,000$ at a pressure of 10^{-4} bar.

3.4 TiO cross-sections

TiO has strong bands in the visible and thus presents a good opportunity to identify the non-LTE effects in the optical, specific for electronic spectra of (diatomic) molecules. For TiO this can be seen in Fig. 19, where more persistent and greater differences between the LTE and non-LTE cases exist; reaching up to 1.89×.

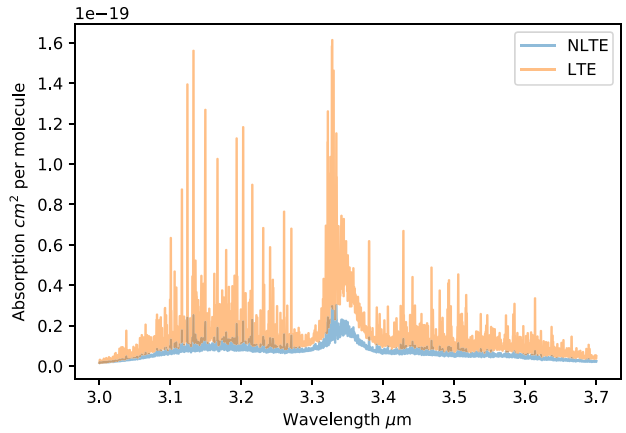

Figure 16. Opacity cross-sections of CH_4 for the second non-LTE scenarios for the band centred around 3.3 μm at $R \sim 150\,000$ at a pressure of 10^{-4} bar.

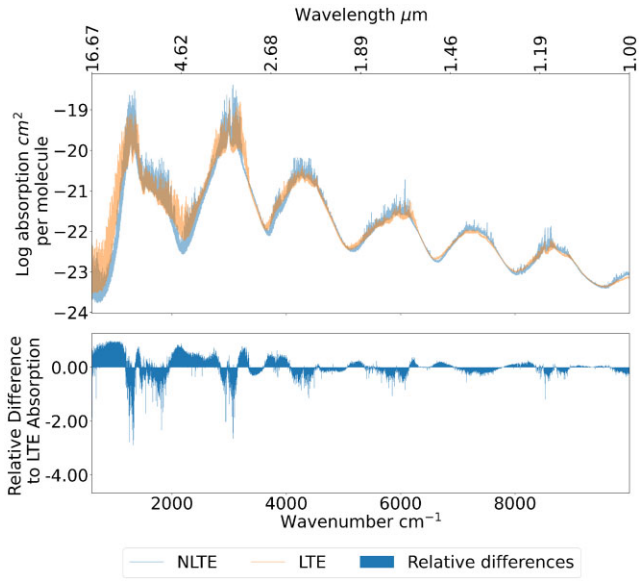

Figure 17. Differences in opacity cross-sections of CH_4 for the first non-LTE scenarios for the band centred around 3.3 μm at $R \sim 150\,000$ at a pressure of 10^{-4} bar.

The optical range is shown for non-LTE scenario 1 in Fig. 20 where substantial differences in absorption can be seen, with a strong absolute level absorption of the order 10^{-15} cm^2 per molecule. The non-LTE bands here absorb far more strongly in the peaks than the LTE bands and incorporate wavelength offsets leading to wider bases (Fig. 19).

The visible region of the TiO absorption is dominated by two electronic bands γ ($A\ ^3\Phi \leftarrow X\ ^3\Delta$) and γ' ($B\ ^3\Pi \leftarrow X\ ^3\Delta$). In Fig. 24, we show the individual contributions from different vibronic bands of TiO in this region. In the LTE absorption spectrum of TiO at $T = 2231$ K the two strongest γ subbands are $v' = 0 \leftarrow v'' = 0$ and $v' = 0 \leftarrow v'' = 1$. Here the lower state energy of $v'' = 1$, X is 999.9 cm^{-1} that is small enough to be significantly populated at $T =$ 2231 K, while the population of the next excited state $v'' = 2$, X ($E = 1990.8$ cm^{-1}) is negligible.

Focussing on the optical range, the differences between LTE and non-LTE can be seen for scenario 2 in Fig. 21. In Fig. 22 the differences between the two cases can be seen over a wider

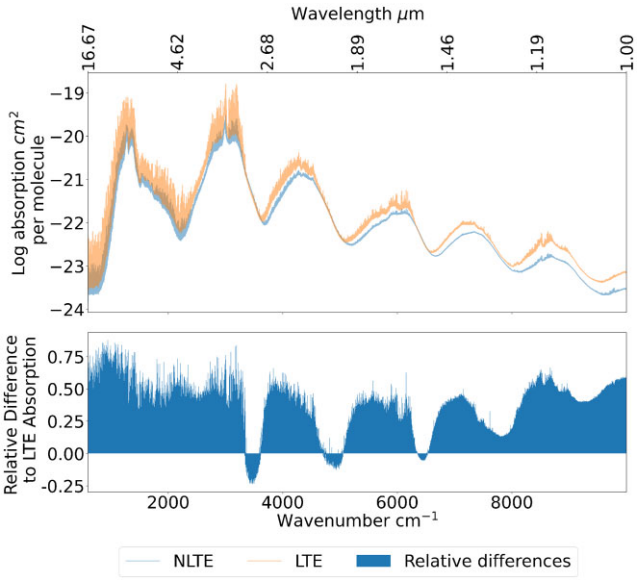

Figure 18. Differences in opacity cross-sections of CH_4 for the second non-LTE scenarios for the band centred around 3.3 μm at $R \sim 150\,000$ at a pressure of 10^{-4} bar.

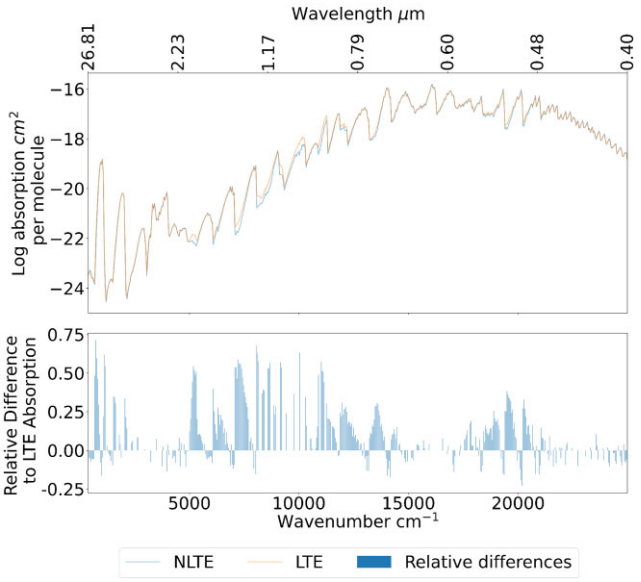

Figure 19. Absorption cross-sections for TiO in LTE and non-LTE at a temperature of 2231 K (with 1800 K for rotational temperature in the non-LTE case) and a pressure of 1 bar and $R \sim 150$. Following our first scenario, with slight rotational cooling of 431 K.

wavelength range along with relative differences; to demonstrate this effect at a higher resolution, Fig. 23 shows a comparison between TiO in LTE and non-LTE scenario 1 at a resolution of $R \sim 150\,000$. From this plot, it can be seen that differences between the two cases extend to as much as 2.07× in the intensity of the band peaks. For the non-LTE spectrum of TiO at $T_{\mathrm{rot}} = 1800$ K and $T_{\mathrm{vib}} = 2231$ K, shown in Fig. 24, the hot γ subbands from the lower excited states $v'' = 2$, X and $v'' = 3$ ($E = 2972.6$ cm^{-1}), X have large enough populations to affect the shape of the spectral band at the longer wavelength, with well-defined signatures.

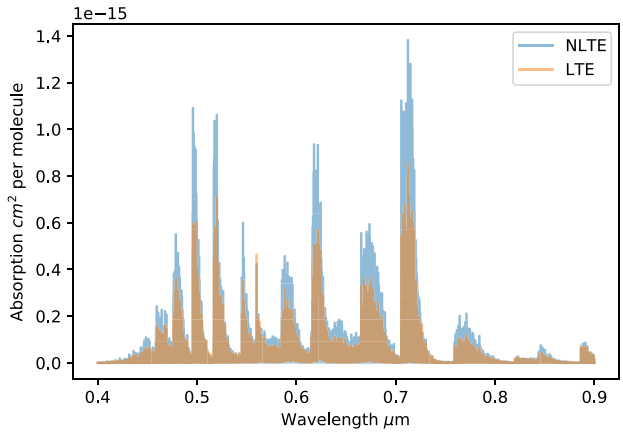

Figure 20. Absorption cross-sections for TiO in LTE and non-LTE at a temperature of 2231 K (with 1800 K for rotational temperature in the non-LTE case) and a pressure of 1 bar with $R \sim 150\,000$ plotted in the visible. Following our first scenario, with slight rotational cooling of 431 K.

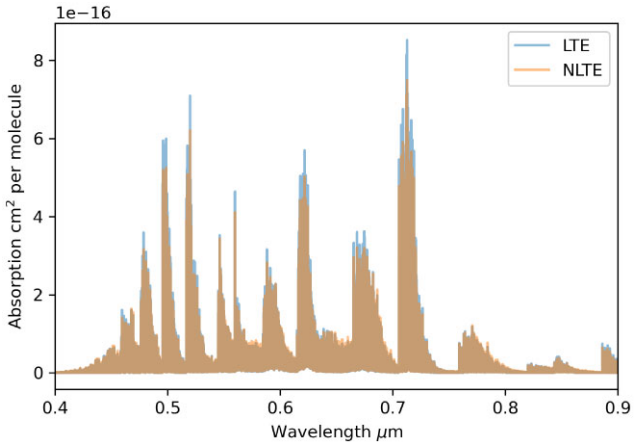

Figure 21. Absorption cross-sections for TiO in LTE and non-LTE at a temperature of 2231 K (with 2662 K for vibrational temperature in the non-LTE case, corresponding to scenario 2) and a pressure of 1 bar and $R \sim 150\,000$.

We should note the recent non-LTE study of thermodynamic and radiative properties of TiO by Bai, Qin & Liu (2021) using high level *ab initio* calculations.

4 DISCUSSION

In all four molecules shown here, CH_4, H_2O, CO, and TiO, there are clear divergences between the absorption cross-sections of the LTE and the non-LTE bi-temperature scenarios assumed here. Under scenario 1, these are driven by a reduction in intensity magnitude of the rotational lines as a result of the cooled rotational degrees of freedom used in opacity generation.

In the polyatomic molecules discussed here (CH_4 and H_2O) this difference manifests as contraction of 'shoulders' of the fundamentals bands in cross-sections for the non-LTE case comparing to LTE, as illustrated for example in Figs 2 and 10. This provides an observable feature that allows the two cases to be spectroscopically distinguished, and where the rotational cooling is sufficient, is even visible by eye. This potential is maximized by focusing on the bands that present the largest differences, for example two spectral regions

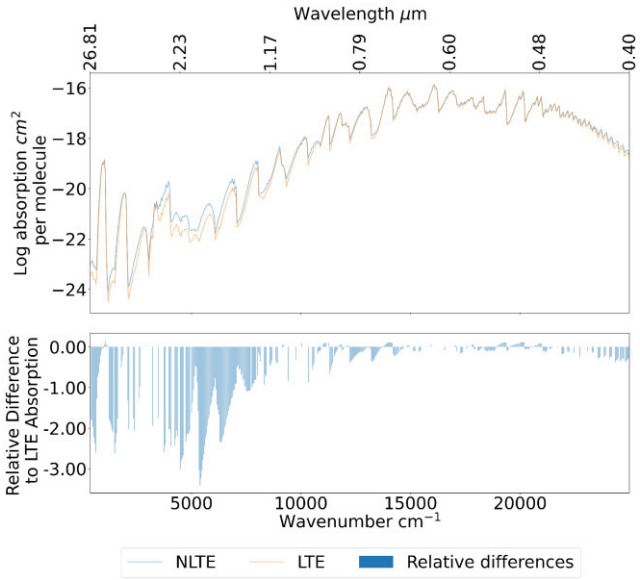

Figure 22. Absorption cross-sections for TiO in LTE and non-LTE at a temperature of 2231 K (with 2662 K for vibrational temperature in the non-LTE case, corresponding to scenario 2) and a pressure of 1 bar with $R \sim 150$ plotted in the visible.

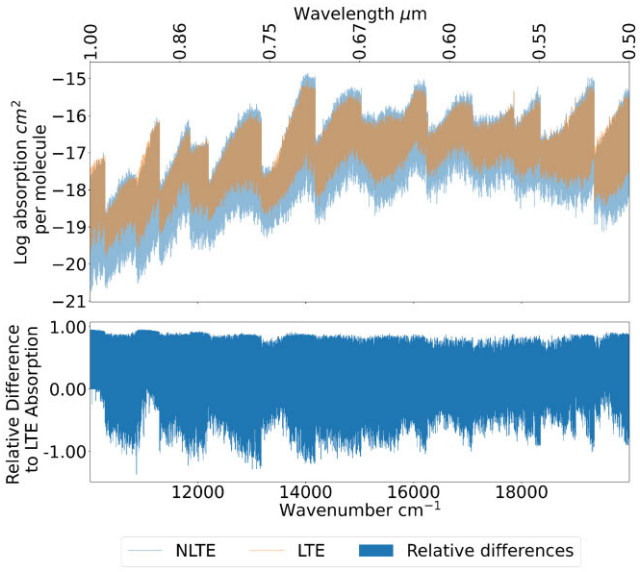

Figure 23. Absorption cross-sections for TiO in LTE and non-LTE at a temperature of 2231 K (with 1800 K for rotational temperature in the non-LTE case, corresponding to scenario 1) and a pressure of 1 bar with $R \sim 150\,000$ plotted between 0.5 and 1 μm.

shown in Fig. 2, and inspecting the relative differences for these regions shown in Fig. 3 illustrates the importance of probing deeper into the IR to observe these effects. This shows the importance of *JWST*'s broader wavelength coverage over *Hubble*'s WFC3 coverage for non-LTE applications. This improved wavelength coverage, coupled with their higher resolving power, *JWST* and ground-based instruments can provide the necessary platforms for spectroscopic studies to distinguish between the LTE and non-LTE as shown here. Analysing the retrieval of non-LTE under this parametrization lies

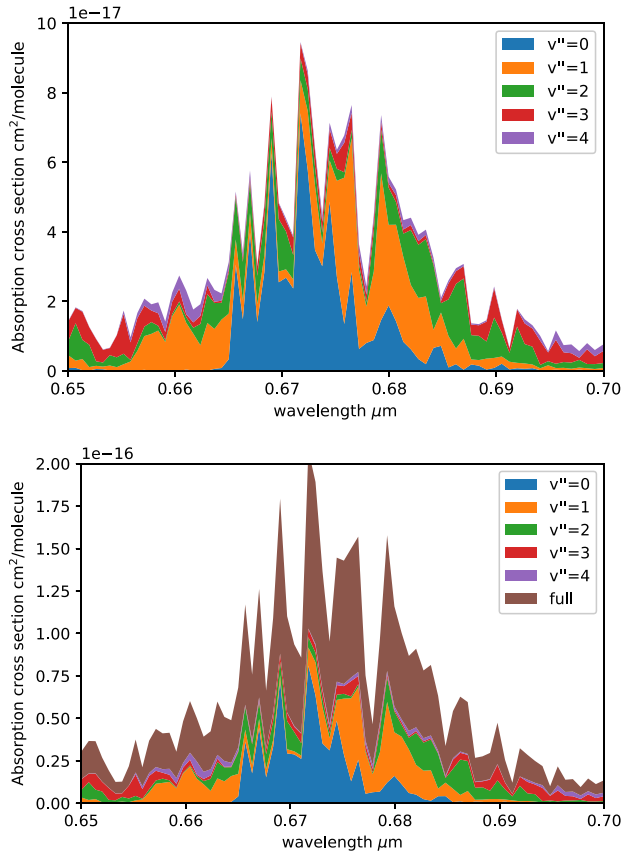

Figure 24. The individual contributions to the γ ($A\,^3\Phi \leftarrow X\,^3\Delta$) and γ' ($B\,^3\Pi \leftarrow X\,^3\Delta$) bands system of TiO from different vibrational bands, LTE and non-LTE (top and bottom plots, respectively). v'' represents the vibrational excitation of the lower state in the ground electronic state $X\,^3\Delta$.

beyond the scope of this publication, future work however will focus on examining retrieval results; where it will be necessary to examine how well retrievals can disentangle non-LTE bi-temperature parameters from additional modelled atmospheric effects under self-retrieval of the model, as well as the retrievability of the bi-temperature parameters under varying non-LTE conditions. This will include evaluating *T–P* profile effects, including bi-temperature pressure profiles that pertain to where and what degree non-LTE effects are introduced under this parametrization.

For the simple diatomic molecule CO considered in this publication, the differences occur as asymmetric offsets around the bands, as shown in Fig. 6. Wavelength offsets such as these present promising opportunities to identify these effects in observed spectra. For CO this must be focused on a viable band however for instance under scenario 1, that which is found in the 3–6 μm range shown in Fig. 6.

The electronic spectra of diatomics represent a special case with the non-LTE vibronic bands shifted relative to each other that help to recognize the non-LTE effects from the appearance of hot satellite bands. This is in contrast to IR, vibrational bands of polyatomic molecule, with the non-LTE bands appearing in the same region as the LTE spectral bands and therefore hidden by them.

Since the non-LTE cross-section modelling process treats the case where rotational and vibrational temperatures are equal as degenerate with the LTE case, it is intuitive that the differences between the two circumstances decrease as the two temperatures converge. A physical effect sufficient to drive a strong enough difference in the energies across these two molecular modes is therefore required to produce a resolvable non-LTE signature in a spectrum observed with the addition of instrumentation error, along with low enough collision rates such that collisions between the molecules do not lead to a strong effective return to LTE.

A number of physical effects could present significant driving forces of these non-LTE conditions at high altitudes in the atmospheres of hot Jupiters, for instance: stellar pumping from a nearby star or shock regions at the boundaries of fast jet streams. In addition, it is known from laboratory experiments that non-LTE effects are important in bow shocks such as those at the boundaries of planetary atmospheres (Scott et al. 2020). Large temperature differentials, such as those common between the dayside and nightside of tidally locked hot Jupiters, can cause very fast jet streams high in the atmosphere (Showman & Polvani 2011). Shock regions form where these jet streams break, with the rotational mode of the molecules cooling preferentially, giving rise to non-LTE conditions; this rotational cooling has been observed experimentally under laboratory conditions. Non-LTE conditions like this are due to the equilibrium between the energies of a molecule's modes breaking down at the normal shock around a supersonic jet (Maté et al. 2001). There are also vertical wind shears in the form of supersonic jets, as suggested to be present in the atmosphere of HD 189733 b (Brogi et al. 2016; Seidel et al. 2020); these fast moving winds with shocks occurring at high altitudes with low pressures present a prime opportunity for the formation and persistence of non-LTE conditions in this manner. In the case of strong stellar irradiation, incoming photons from the host star excite the vibrational molecular mode preferentially; this is referred to as 'pumping' and may drive molecules to non-LTE states even at lower altitudes (Feofilov & Kutepov 2012). In the laboratory setting, plasma glow discharges have produced vibrational excitation in CO_2 (Klarenaar et al. 2017) where the vibrational temperature is recorded at 550 K over the rotational temperature. To name a few examples within our own Solar system, in Earth's atmosphere, non-LTE effects are present with visible effects in the form of airglow emissions, as noted for vibrationally excited OH in Charters, Macdonald & Polanyi (1971), for which level populations have been measured (Noll et al. 2020). In the atmosphere of Mars, CO_2 has a non-LTE emission feature at 4.3 μm (López-Valverde et al. 2005; Giuranna et al. 2018). In the atmosphere of Venus non-LTE emissions have been detected in limb observations for CO (Gilli et al. 2015) and CO_2 (Gilli et al. 2009). For CH_4 (García-Comas et al. 2011) and HCN (Rezac et al. 2013) in Titan's atmosphere and for CH_4 in the atmospheres of Jupiter and Saturn (Drossart et al. 1999).

5 CONCLUSION

A simplified bi-temperature model for non-LTE spectra of exoplanetary atmospheres is used to investigate features of vibrational bands to produce non-LTE spectral signatures for four key atmospheric molecules, CH_4, H_2O, CO, and TiO. These molecules sample different spectra ranges (IR and visible), different spectral types (electronic and rovibrational), and different molecular types (diatomics and polyatomics). In the case of the visible spectrum of the diatomic molecule TiO, it can be seen that the hot bands are shifted from the main, most-populated band, which makes it easier to distinguish and also to use as a non-LTE indicator. For the (non-linear) polyatomics, the hot bands sit on top of each, making their recognition more challenging. Still, the shapes of the non-LTE bands show differences that should be significant enough to make them detectable.

It can be seen from this investigation that the presence of CH_4, H_2O, CO, and TiO molecules in a state of non-LTE can be

distinguished from their presence in LTE by way of variations in their absorption relative to each other. This underlying variation in the spectroscopic characteristics of the molecules based on the state of their LTE is a method by which such effects could potentially be detected.

Among this sample of molecules, differences in both the optical and IR regions of the spectrum can be seen, indicating the potential for detection of these effects with multiple observing methods including *JWST* and ground-based high-resolution facilities.

Across the molecules, a number of prominent signatures emerge to distinguish non-LTE. For instance CH_4 has a prominent signature where the LTE and scenario 1 non-LTE absorption cross-sections diverge around 3.15 μm – this shift of the *R* branch gives a distinctive spectral feature by which to distinguish CH_4 in non-LTE. Under scenario 2, absorption variations exist across the board giving a noticeable difference. While for H_2O, such signatures are exhibited as an absence of shoulders around the 2.0 and 2.7 μm bands for scenario 1. The sole strong carbon monoxide signature for scenario 1 non-LTE is visible as an offset between 5 and 6 μm, while additional strong offsets exist for scenario 2 vibrational excitation around the 2.76 and 1.75 μm bands. In the case of TiO numerous strong signatures exist in the optical part of the spectrum, present in the bands distributed between 0.5 and 0.75 μm, most notably for rotational cooling. The nature of the non-LTE manifestation for the electronic spectrum of TiO is different from the IR spectra of H_2O, CH_4, or CO: it manifests as intensity variations of the vibronic bands rather than contraction of the band shoulders for the rovibrational spectra. The result is that the non-LTE versus LTE differences are intuitively visible as a narrowing of the bands for H_2O, CH_4, and CO, and as higher peaks for TiO.

Non-LTE can, and does, arise frequently in planetary atmospheres in a variety of scenarios. Rather than examine each of these cases individually (if indeed it is tractable), the model presented here describes the aggregate non-LTE effect via the bi-temperature parametrization that is used in many cases. Taking separate rotational and vibrational temperatures as parameters for a two Boltzmann temperature model provides a robust and efficient approach to introducing this additional degree of freedom with which to model non-LTE spectral effects, while the form of the additional temperature dependence term can be further explored. In this way non-LTE absorption characteristics can be determined for molecules with this two-temperature model, without the need to explicitly calculate non-LTE population densities that require a priori knowledge of specific physical mechanisms within atmospheric scenarios so detailed as to be incompatible with the exoplanet use case.

6 FURTHER WORK

Further work on this topic will investigate non-LTE effects in high-resolution exoplanet spectra. In addition, this non-LTE approach will be investigated as an addition to traditional retrieval frameworks, using the same non-LTE cross-section approximations to introduce additional fitted temperature variables. This will seek to quantify the degree to which an observed spectrum can be explained by a given molecule existing in a state of non-LTE. Additional work will look into modelling of the dayside–nightside temperature dynamics to place additional constraint on the differences in molecular rotational and vibrational temperatures caused by physical conditions, as well as atmospheric pressure constraints driving molecular populations back to LTE.

ACKNOWLEDGEMENTS

SOMW was supported by the STFC UCL Centre for Doctoral Training in Data Intensive Science (grant number ST/P006736/1) This project has received funding from the European Research Council (ERC) under the European Union's Horizon 2020 Framework Programme (grant agreement no. 758892, ExoAI), the European Union's Horizon 2020 Framework Programme COMPET programme (grant agreement no. 776403, ExoplANETS A), and the ERC Advanced Grant Project No. 883830. Furthermore, we acknowledge funding by the UK Space Agency and Science and Technology Funding Council (STFC) grants: ST/R000476/1, ST/K502406/1, ST/P000282/1, ST/P002153/1, ST/S002634/1, and ST/T001836/1. The authors acknowledge the use of the UCL Legion High Performance Computing Facility (Legion@UCL) and associated support services in the completion of this work, along with the Cambridge Service for Data Driven Discovery (CSD3), part of which is operated by the University of Cambridge Research Computing on behalf of the STFC DiRAC HPC Facility (www.dirac.ac.uk). The DiRAC component of CSD3 was funded by BEIS capital funding via STFC capital grants ST/P002307/1 and ST/R002452/1 and STFC operations grant ST/R00689X/1. DiRAC is part of the National e-Infrastructure.

Software used: EXOCROSS (Yurchenko et al. 2018), TAUREX3 (Al-Refaie et al. 2021), NUMPY (Harris et al. 2020), PANDAS, H5PY, and MATPLOTLIB (Hunter 2007).

DATA AVAILABILITY

The underlying molecular line list data from the ExoMol project are available from the ExoMol website (www.exomol.com). Derived non-LTE data are available from the corresponding author upon reasonable request.

REFERENCES

Al-Refaie A. F., Changeat Q., Waldmann I. P., Tinetti G., 2021, ApJ, 917, 37
Appleby J. F., 1990, Icarus, 85, 355
Arcangeli J., Désert J.-M., Parmentier V., Tsai S.-M., Stevenson K. B., 2021, A&A, 646, A94
Bai T., Qin Z., Liu L., 2021, Mol. Phys., 119, e1953174
Bell T. J. et al., 2019, MNRAS, 489, 1995
Brogi M., de Kok R. J., Albrecht S., Snellen I. A. G., Birkby J. L., Schwarz H., 2016, ApJ, 817, 106
Butterworth T., van de Steeg A., van den Bekerom D., Minea T., Righart T., Ong Q., van Rooij G., 2020, Plasma Sources Sci. Technol., 29, 095007
Charters P. E., Macdonald R. G., Polanyi J. C., 1971, Appl. Opt., 10, 1747
Clark V. H. J., Yurchenko S. N., 2021, Phys. Chem. Chem. Phys., 23, 11990
Curtis A., Goody R., 1956, Proc. Math. Phys. Eng., 236, 193
Dickinson R. E., 1972, J. Atmos. Sci., 29, 1531
Drossart P., 2019, Philos. Trans. R. Soc. A, 377, 20180404
Drossart P., Fouchet T., Crovisier J., Lellouch E., Encrenaz T., Feuchtgruber H., Champion J. P., 1999, in Cox P., Kessler M. F., eds, ESA Special Publication Vol. 427, The Universe as Seen by *ISO*. ESA, Noordwijk, p. 169
Dudás E., Suas-David N., Brahmachary S., Kulkarni V., Benidar A., Kassi S., Charles C., Georges R., 2020, J. Chem. Phys., 152, 134201
Edwards B. et al., 2020, AJ, 160, 8
Feofilov A. G., Kutepov A. A., 2012, Surv. Geophys., 33, 1231
Fisher C., Heng K., 2019, ApJ, 881, 25
Funke B., López-Puertas M., García-Comas M., Kaufmann M., Höpfner M., Stiller G., 2012, J. Quant. Spectrosc. Radiat. Transf., 113, 1771
García-Comas M., López-Puertas M., Funke B., Dinelli B. M., Luisa Moriconi M., Adriani A., Molina A., Coradini A., 2011, Icarus, 214, 571

Gilli G., López-Valverde M. A., Drossart P., Piccioni G., Erard S., Cardesín Moinelo A., 2009, J. Geophys. Res., 114, E00B29
Gilli G., López-Valverde M., Peralta J., Bougher S., Brecht A., Drossart P., Piccioni G., 2015, Icarus, 248, 478
Giuranna M., Fonte S., Longobardo A., Sindoni G., Wolkenberg P., Formisano V., 2018, Icarus, 315, 46
Goldsmith P. F., Langer W. D., 1999, ApJ, 517, 209
Harris C. R. et al., 2020, Nature, 585, 357
Houghton J., 1969, Q. J. R. Meteorological Soc., 95, 1
Hunter J. D., 2007, Comput. Sci. Eng., 9, 90
Kaminski T., Schmidt M. R., Menten K. M., 2013a, A&A, 549, A6
Kaminski T. et al., 2013b, A&A, 551, A113
Kim S. J., Sim C. K., Ho J., Geballe T. R., Yung Y. L., Miller S., Kim Y. H., 2015, Icarus, 257, 217
Klarenaar B. L. M., Engeln R., van den Bekerom D. C. M., van de Sanden M. C. M., Morillo-Candas A. S., Guaitella O., 2017, Plasma Sources Sci. Technol., 26, 115008
Koskinen T. T., Aylward A. D., Miller S., 2007, Nature, 450, 845
Kuhn W. R., London J., 1969, J. Atmos. Sci., 26, 189
Kumer J. B., James T. C., 1974, J. Geophys. Res., 79, 638
Li G., Gordon I. E., Rothman L. S., Tan Y., Hu S.-M., Kassi S., Campargue A., Medvedev E. S., 2015, ApJS, 216, 15
Lique F., van der Tak F., Klos J., Bulthuis J., Alexander M., 2009, A&A, 493, 557
López-Puertas M., Taylor F. W., 2001, Non-LTE Radiative Transfer in the Atmosphere. World Scientific Press, Singapore
López-Puertas M., Rodrigo R., Molina A., Taylor F., 1986a, J. Atmos. Terr. Phys., 48, 729
López-Puertas M., Rodrigo R., López-Moreno J., Taylor F., 1986b, J. Atmos. Terr. Phys., 48, 749
López-Valverde M., López-Puertas M., López-Moreno J., Formisano V., Grassi D., Maturilli A., Lellouch E., Drossart P., 2005, Planet. Space Sci., 53, 1079
López-Valverde M., Drossart P., Carlson R., Mehlman R., Roos-Serote M., 2007, Planet. Space Sci., 55, 1757
Mandell A. M., Deming L. D., Blake G. A., Knutson H. A., Mumma M. J., Villanueva G. L., Salyk C., 2011, ApJ, 728, 18
Maté B., Graur I. A., Elizarova T., Chirokov I., Tejeda G., Fernández J. M., Montero S., 2001, J. Fluid Mech., 426, 177
May E. M. et al., 2021, AJ, 162, 158
Milne E. A., 1930, Handbuch der Astrophysik, Vol. 3, Grundlagen der Astrophysik. Springer-Verlag, Berlin, p. 65
Noll S., Winkler H., Goussev O., Proxauf B., 2020, Atmos. Chem. Phys., 20, 5269
Pannier E., Laux C. O., 2019, J. Quant. Spectrosc. Radiat. Transf., 222, 12
Rezac L., Kutepov A. A., Faure A., Hartogh P., Feofilov A. G., 2013, A&A, 555, A122
Scott R. H. H. et al., 2020, Phys. Plasmas, 27, 033301
Seidel J. V., Ehrenreich D., Pino L., Bourrier V., Lavie B., Allart R., Wyttenbach A., Lovis C., 2020, A&A, 633, A86
Showman A. P., Polvani L. M., 2011, ApJ, 738, 71
Shved G., 1975, SvA, 18, 499
Stiller G. P., von Clarmann T., Funke B., Glatthor N., Hase F., Höpfner M., Linden A., 2002, J. Quant. Spectrosc. Radiat. Transf., 72, 249
Swain M. R. et al., 2010, Nature, 463, 637
Swain M. et al., 2013, Icarus, 225, 432
Tennyson J. et al., 2020, J. Quant. Spectrosc. Radiat. Transf., 255, 107228
Treanor C. E., Rich J. W., Rehm R. G., 1968, J. Chem. Phys., 48, 1798
van der Tak F., Black J., Schöier F., Jansen D., van Dishoeck E., 2007, A&A, 468, 627
Van de Sande M., Decin L., Lombaert R., Khouri T., de Koter A., Wyrowski F., De Nutte R., Homan W., 2018, A&A, 609, A63
Waldmann I. P., Tinetti G., Drossart P., Swain M. R., Deroo P., Griffith C. A., 2012, ApJ, 744, 35
Weaver H. A., Mumma M. J., 1984, ApJ, 276, 782
Wintersteiner P. P., Picard R. H., Sharma R. D., Winick J. R., Joseph R. A., 1992, J. Geophys. Res., 97, 18083
Yee S. W. et al., 2019, ApJ, 888, L5
Yurchenko S. N., Tennyson J., 2014, MNRAS, 440, 1649
Yurchenko S. N., Al-Refaie A. F., Tennyson J., 2018, A&A, 614, A131

This paper has been typeset from a TEX/LATEX file prepared by the author.